The Journal of Chemical Physics

Fermi level dependence of gas–solid oxygen defect exchange mechanism on TiO_2 (110) by first-principles calculations

Cite as: J. Chem. Phys. **153**, 124710 (2020); https://doi.org/10.1063/5.0023180
Submitted: 27 July 2020 . Accepted: 08 September 2020 . Published Online: 28 September 2020

Heonjae Jeong, Edmund G. Seebauer, and Elif Ertekin

The Journal of Chemical Physics ARTICLE scitation.org/journal/jcp

Fermi level dependence of gas–solid oxygen defect exchange mechanism on TiO_2 (110) by first-principles calculations

Cite as: J. Chem. Phys. 153, 124710 (2020); doi: 10.1063/5.0023180
Submitted: 27 July 2020 • Accepted: 8 September 2020 •
Published Online: 28 September 2020

Heonjae Jeong,[1] Edmund G. Seebauer,[2] and Elif Ertekin[1,a)]

AFFILIATIONS

[1] Department of Mechanical Science and Engineering, University of Illinois at Urbana-Champaign, Urbana, Illinois 61801, USA
[2] Department of Chemical and Biomolecular Engineering, University of Illinois at Urbana-Champaign, Urbana, Illinois 61801, USA

[a)] Author to whom correspondence should be addressed: ertekin@illinois.edu

ABSTRACT

In the same way that gases interact with oxide semiconductor surfaces from above, point defects interact from below. Previous experiments have described defect–surface reactions for TiO_2(110), but an atomistic picture of the mechanism remains unknown. The present work employs computations by density functional theory of the thermodynamic stabilities of metastable states to elucidate possible reaction pathways for oxygen interstitial atoms at TiO_2(110). The simulations uncover unexpected metastable states including dumbbell and split configurations in the surface plane that resemble analogous interstitial species in the deep bulk. Comparison of the energy landscapes involving neutral (unionized) and charged intermediates shows that the Fermi energy E_F exerts a strong influence on the identity of the most likely pathway. The largest elementary-step thermodynamic barrier for interstitial injection trends mostly downward by 2.1 eV as E_F increases between the valence and conduction band edges, while that for annihilation trends upward by 2.1 eV. Several charged intermediates become stabilized for most values of E_F upon receiving conduction band electrons from TiO_2, and the behavior of these species governs much of the overall energy landscape.

I. INTRODUCTION

In the same way that gases interact with surfaces from above by adsorption and desorption, point defects interact from below by annihilation and injection. For metal oxide semiconductors, surface chemistry from above has been long-studied for applications in photocatalysis,[1,2] gas sensing,[3,4] optoelectronics manufacture,[5,6] and many others. There are several existing experimental and computational analyses of the interaction between surfaces and gas molecules, including oxygen,[7–11] hydrogen,[12,13] carbon monoxide,[14,15] and methanol.[16,17] However, reactions with defects that range from a surface to a subsurface have drawn comparatively little attention. Mounting evidence for oxide semiconductors suggests that chemistry from below exhibits richness comparable to reactions with gases and offers a useful means for regulating defect behavior. For example, removing adsorbed foreign-atom poisons from the surfaces of TiO_2 and ZnO enables the majority O-related defect to be altered.[18–22]

Little *a priori* understanding exists regarding the likely mechanisms, rate expressions, and temperature dependences of defect–surface interactions. Experiments coupled with mesoscale modeling[23–26] over length scales of 3 nm–500 nm have provided significant but limited insights. Among semiconducting oxides, TiO_2(110) represents the best-understood system with a physical picture for surface exchange that includes[22–25] anion and cation defects (i.e., O and Ti) as modulated by the Fermi energy E_F and extended defect sequestration sites. This literature base makes TiO_2(110) especially suitable for atomistic first-principles elucidation of likely reaction mechanisms. Specifically, prior experiments[22–25] have shown that TiO_2(110) surfaces mediate exchange with subsurface oxygen interstitials O_i. While there is now ample evidence of an active oxygen defect exchange mechanism occurring at the (110) rutile

TiO_2 surface resulting in injection or annihilation of O_i, the precise atomic scale mechanism by which it occurs is presently not known.

The present work employs density functional theory (DFT) calculations for this purpose, focusing on the thermodynamic stability of metastable states along the exchange reaction pathway. The simulations reveal unanticipated metastable states in the surface plane that include dumbbell and split configurations resembling interstitial species in the deep bulk. Comparison of thermodynamic pathways involving neutral (unionized) and charged intermediates shows that E_F exerts a strong influence on the identity of the most likely pathway—a feature that we surmise characterizes most semiconductors that support point defects capable of adopting distinct charge states with disparate atomic geometries. The largest elementary-step thermodynamic barrier for interstitial injection trends mostly downward by 2.1 eV as E_F increases between the valence and conduction band (CB) edges, while that for annihilation trends upward by 2.1 eV. Several charged intermediates become stabilized for most values of E_F upon receiving conduction band electrons from TiO_2, and the behavior of these species governs much of the overall energy landscape.

Overall, this analysis (i) identifies a plausible atomistic mechanism and reaction pathway for our prior experiments and (ii) shows that the semiconductor Fermi energy plays a significant role in tuning the reaction energy landscape for the hypothesized pathway. Many studies of energy landscapes for adsorbate behavior on semiconductors neglect the possibility of charge transfer.[27–29] By contrast, the present study accounts for that possibility using an artificial doping procedure involving a vacancy placed at the backside of the simulation slab and generalizing the numerical results to the arbitrary Fermi energy. This analysis suggests that the semiconductor Fermi energy can have a significant impact on measured activation energies and that such charge transfer should be considered when analyzing reaction energy landscapes and comparing to the experiment.

II. METHODS

A. Computational method and slab geometry

DFT calculations were performed using the Vienna *Ab Initio* Simulation Package (VASP)[30,31] with projector augmented wave (PAW)[32] pseudopotentials and the Perdew–Burke–Ernzerhof (PBE)[33] generalized gradient approximation (GGA) to the exchange–correlation functional. The plane-wave energy cutoff was 520 eV. For all configurations, geometry optimization was carried out until the residual force on each atom fell below 0.01 eV/Å.

We simulated defect exchange through the (110) (1 × 1) rutile TiO_2 surface reconstruction that prevails at the experimental conditions[18,19,23,25] of $T = 973$ K and $P_{O_2} = 1 \times 10^{-5}$ Torr. Figure 1(a) illustrates this surface, which exposes oxygen in twofold (O_{2f}) and threefold (O_{3f}) coordination as well as titanium in fivefold (Ti_{5f}) coordination. The slab contained nine tri-layers ($O–Ti_2O_2–O$) allowing for a net charge-neutral stoichiometry[34] and sufficient to converge surface energies (see Fig. S1 in the supplementary material). A 15 Å vacuum region was included to isolate each slab from its images arising from periodic boundary conditions. To simulate the defect exchange process, a 2 × 2 supercell was used in the lateral direction, and the Brillouin zone was sampled with a 3 × 3 × 1 Monkhorst–Pack k-point mesh.

B. Total energy change for O_i creation from O_2 gas phase

The total energy change for creating two O_i in the bulk from a gaseous O_2 molecule is given by $2\Delta E_f$, where ΔE_f is the formation energy of one oxygen interstitial,[35]

$$\Delta E_f = (E_{O_i,q} - E_{TiO_2}) - \left(\frac{1}{2}\right)\mu_{O_2} + q(E_V + E_F). \quad (1)$$

Here, $E_{O_i,q}$ is the DFT-computed total energy of a TiO_2 supercell containing an O_i defect in charge state q, E_{TiO_2} is the DFT-computed total energy of the same supercell without the defect, μ_{O_2} is the oxygen molecule chemical potential, E_V is the energy of the valence band maximum (VBM), and E_F is the Fermi level referenced to the VBM. With the semiconductor bandgap denoted as E_g, E_F obeys $0 < E_F < E_g$. Figure S2 in the supplementary material shows ΔE_f as a function of Fermi energy E_F reproduced from our prior work.[36] For $E_F < 0.9$ eV, O_i is stable in the neutral charge state (q = 0), and the overall reaction energy to form two O_i is 5.36 eV. For Fermi energies $E_F > 0.9$ eV, the stable charge state of O_i is $q = -2$. This means that the total energy change decreases with increasing Fermi energy, necessitating that the overall thermodynamic reaction energy landscape must also depend on E_F.

We note that there are well-known limitations to the use of DFT-PBE and Eq. (1) to describe point defect energetics in semiconductors due to the underestimated bandgap and the tendency of PBE to overly delocalize defect levels. In our prior work[36] and here, we apply the approach outlined in Ref. 37 to estimate corrections for the underestimated PBE bandgap, positions of defect levels, and finite size effects. By doing so, we can reproduce formation energies and charge transition levels as determined from hybrid functional DFT[38,39] to within ~0.2 eV. We, therefore, surmise that residual uncertainties in the results presented here are likely of the same order, around 0.2 eV–0.3 eV. Since the reaction energy landscapes that we report in the results vary with Fermi energy to a much greater extent of ~2 eV, we do not expect that the main findings and conclusions of our work will be affected by the choice of functional here.

C. Configuration energies for neutral and charged species

If a configuration is charge neutral, its energy is given by

$$\Delta E_{conf} = \left(E_{conf}^{slab} - E_{TiO_2}^{slab}\right) - (n/2)\mu_{O_2}, \quad (2)$$

where E_{conf}^{slab} is the DFT energy of the configuration, $E_{TiO_2}^{slab}$ is the DFT-computed total energy of the pristine slab, and n denotes the number of excess oxygen atoms present in the configuration relative to the pristine slab.

For $E_F > 0.9$ eV, the most stable deep-bulk species is O_i^{2-}, implying that each interstitial exchanges two electrons net with the semiconductor during injection or annihilation. DFT simulations typically do not include charged configurations in periodic

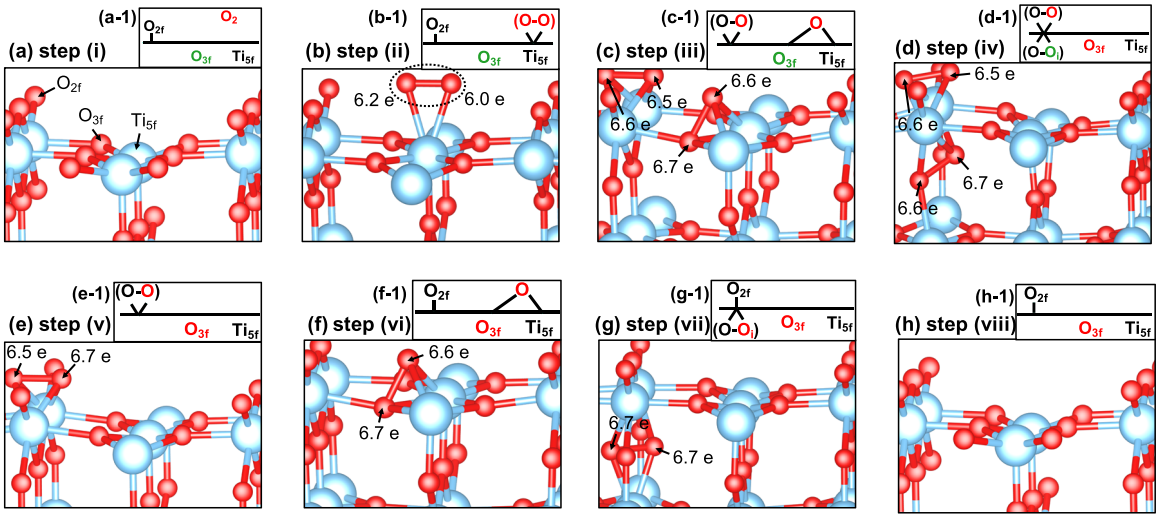

FIG. 1. Sequential steps for the injection of two neutral O_i through TiO_2(110), which entails O_2 adsorption, dissociation, and two O injections. (a)–(h) show the reaction intermediates for the injection of two neutral O_i. Annihilation entails movement through the sequence in the reverse order. Insets (a-1)–(h-1) above the atomic geometries show each step schematically; atoms marked in red originate from the gas phase and the blue atom originates from the surface O_{3f} that is exchanged by adsorbates. The configurations shown are as follows: (a) gaseous O_2 and the pristine TiO_2 (110) surface, (b) the adsorption of O_2 on Ti_{5f}, (c) dissociation of O_2 leaving an O_{ads} on both O_{2f} and O_{3f}, resulting in the formation of surface dumbbell interstitial above O_{3f}, (d) consecutive motion of the surface O_{3f} into the subsurface and surface interstitial into O_{3f}, resulting in a formation of subsurface dumbbell interstitial below O_{2f}, (e) diffusion of subsurface O_i into the deep bulk, (f) formation of the second surface dumbbell interstitial above O_{3f} via motion of remaining O_{ads} from O_{2f}, (g) its injection into the subsurface and the formation of dumbbell O_i below O_{2f}, and (h) diffusion of the second O_i into the deep bulk.

slab calculations because of significant technical challenges. For charged slabs, periodic boundary conditions result in spurious electrostatic interactions between the charge and its images, which cause the computed total energy to diverge artificially with increasing vacuum region length. The accurate calculation of the formation energy for a charge species together with the dependence upon E_F requires proper accounting for these interactions. Establishing rigorous approaches for this accounting remains an active area of research.[40–42]

Here, we account for the possibility of charged configurations in an approximate way by "doping" the slab to provide a reservoir of conduction band electrons that can transfer to metastable species whenever that is energetically favorable. Slightly different, but related methods of artificial doping have been recently reported elsewhere.[43,44] We accomplish doping by adding an oxygen vacancy V_O to the backside of the slab with the sole purpose of providing conduction band electrons for exchange with defect-related species at the slab's front surface.

Previous literature indicates that TiO_2(110) surface vacancies exhibit two stable charge states: a q = +2 donor state and a q = 0 neutral state. The q = +1 state is also possible but is only metastable.[45] As shown from the density of states in the supplementary material (Fig. S3), a V_O at the backside introduces two delocalized electrons that reside in a perturbed host state of the TiO_2 conduction band (CB). Whenever energetically favorable, one or two of these electrons transfer to the defect-related species, leaving a net positive charge on the backside V_O and a net negative charge on the defect species. The supercell as a whole remains neutral.

This approach requires two operations in order to determine the stability of a charged front-surface intermediate. First, the number of electrons, q_{tr}, transferred from the backside V_O to the reaction intermediate must be evaluated. We ascertain q_{tr} through the examination of the Bader charges and the density of states. This parameter takes on values of 0, 1, or 2 for the metastable states considered here and is not externally set but rather determined within the DFT simulation. Second, the ionization contribution to the configuration energy for non-zero values of q_{tr} must be evaluated. The configuration energy returned by the DFT simulation corresponds only to the specific value of E_F that prevails within the calculation. However, we need to understand how the configuration energy varies over wide ranges of E_F. We do this by modifying Eq. (2) above to include a term that contains an arbitrarily chosen value of E_F as follows:

$$\Delta E_{conf} = \left(E_{conf}^{slab+V_O} - E_{TiO_2}^{slab+V_O}\right) - (n/2)\mu_{O_2} + q_{tr}\Delta E_{F,offset}. \quad (3)$$

Here, $\Delta E_{F,offset} = E_F - E_F^{DFT}$ denotes the mathematical offset between the Fermi energy E_F^{DFT} that happens to prevail within the DFT calculation and the real-system Fermi energy E_F. Since the two electrons introduced by the backside V_O effectively reside at the conduction band minimum (CBM), then E_F^{DFT} = 1.55 eV corresponding to the value of the slab's PBE bandgap.

The artificial doping method and the accounting procedure for E_F entail approximations and rely on several assumptions. For example, one key assumption is that the defect level of the backside vacancy is sufficiently delocalized in the conduction bands

that the energy to remove an electron is well-represented by the Kohn–Sham eigenvalue of the defect level so that Eq. (3) can be used. Figures S2 and S3 in the supplementary material and the accompanying text describe those assumptions in detail. The accuracy of the approach may be assessed by comparing the energy of O_i^{2-} in the middle of a slab having V_O doping to the corresponding energy computed with the usual charged supercells in the bulk. The discussion in the supplementary material shows that the doped TiO_2 slabs yield satisfactory accuracy. In the supplementary material, Figs. S4–S7, we also use PBE + U and present an analysis of the sensitivity of the density of states and the charge transfer q_{tr} to the value of U for several reaction steps. We find that the results remain consistent provided that U is not set to an unphysically large value around U = 5 eV. If the value of U becomes too large, then the backside vacancy becomes more localized and the energy to add an electron to the defect level is no longer well-described by the Kohn–Sham eigenvalue. Since the results we report are obtained using PBE with estimated corrections for the bandgap and defect levels, this observation does not affect our reported trends or conclusions.

D. Reaction energy pathway

Although the exchange between O_2 gas and deep-bulk O_i transpires in both directions and entails both injection and annihilation of O_i at the surface, the present analysis for convenience defines the reaction coordinate in the injection direction—separately highlighting important results for annihilation. The conversion of gaseous O_2 into two O_i atoms is simulated by an assumed sequence of elementary steps between metastable configurations, with one interstitial injecting after the other. To analyze the injection energy landscape, the intermediate surface configurations are simulated and their sequential energies tracked to produce thermodynamic landscape "staircase" diagrams. Although other possible pathways may exist, we assume the following sequence of intermediate reactions here: adsorption of O_2, its dissociation, and then two successive injection events of O atoms from the surface to the subsurface layer. We did consider an alternative sequence in which a lattice O at the surface first injects into the interior as an interstitial and leaves behind a surface vacancy after which O_2 becomes adsorbed at the vacant surface site. However, this reaction sequence generally resulted in higher thermodynamic barriers and so is described in detail only in the supplementary material.

All configurations shown in this paper correspond to metastable states along the injection pathway. Since kinetic barriers between reaction intermediates are neglected,[46–49] our analysis provides a useful but incomplete picture of the injection reaction. These barriers will be described separately in a forthcoming study.[50]

III. RESULTS AND DISCUSSION

A. Neutral O_i

Figure 2 shows the staircase diagram for the reaction pathway for the injection of neutral O_i, shown for our prior experimental condition of T = 973 K and $P_{O_2} = 1 \times 10^{-5}$ Torr (corresponding to $\Delta\mu_{O_2} = -1.3$ eV with $\mu_{O_2} = \mu_{O_2}^{DFT} + \Delta\mu_{O_2}$). The maximum energy change of 3.35 eV is quite large and occurs between steps (i) and(ii), corresponding to the adsorption of O_2 on Ti_{5f}. The subsequent steps present smaller thermodynamic barriers, although except for a slight decline in steps (v) → (vi), the reaction proceeds entirely uphill to realize the net energy change of 5.36 eV corresponding to the total energy change for the injection of two neutral O_i. Figure 2 shows that the reverse process of annihilation proceeds almost entirely downhill.

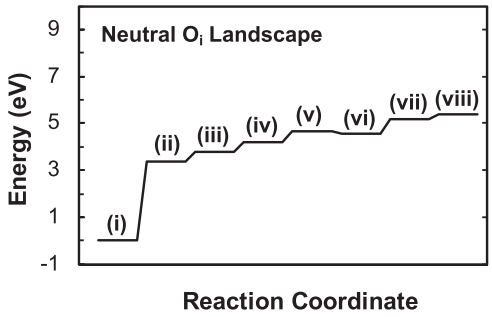

FIG. 2. Reaction energy diagram for the injection of two neutral O_i atoms under the experimental condition of $\Delta\mu_{O_2} = -1.3$ eV (T = 973 K and $P_{O_2} = 1 \times 10^{-5}$ Torr). Rightward movement along the reaction coordinate corresponds to injection; annihilation proceeds leftward. Steps (i)–(viii) correspond to the configurations detailed in Fig. 1.

B. Charged O_i

Figure 3 shows the schematics of the sequential configurations for the exchange of charged O_i with the associated value of q_{tr} for each configuration. A detailed discussion for each step is provided in Figs. S3 and S4 of the supplementary material. Notably, with the backside vacancy present, O_i adopts a q = −2 charge state for most steps. This is shown in Figs. 3(b)–3(f), where the distance between and the Bader charges on the two oxygen atoms has substantially changed in comparison to Fig. 1. The defect-related species here adopt configurations and Bader charges resembling the split interstitial O_i in the bulk. That bulk species carries a charge of −2 and occurs for $E_F > 0.9$ eV.[36]

The version of this species residing in the surface plane at an $O_{ads,3f}$ site may be termed a "surface split" by analogy to the surface dumbbell described above. This surface split lacks an O–O bond and serves as a conduit by which the injection of charged O_i^{2-} occurs. The existence of this configuration is perhaps surprising, but as with the surface dumbbell, the low spatial density of atoms in the first sublayer provides sufficient space for a distorted analog of the bulk split to form.

The only two configurations in Fig. 3 for which $q_{tr} \neq 2$ occur for Fig. 3(a) for which $q_{tr} = 1$ and Fig. 3(d) for which $q_{tr} = 0$. Figure 3(a) corresponds to the adsorption of the O_2 at the Ti_{5f} site for which we find $q_{tr} = 1$. This observation indicates that to ultimately form two O_i^{2-} in the subsurface from gaseous O_2, the first electron is transferred during the adsorption of O_2 [Fig. 3(a)] and the second during its dissociation [Fig. 3(b)]. These first two electrons travel together with the injected O_i as it diffuses into the bulk, leaving the surface

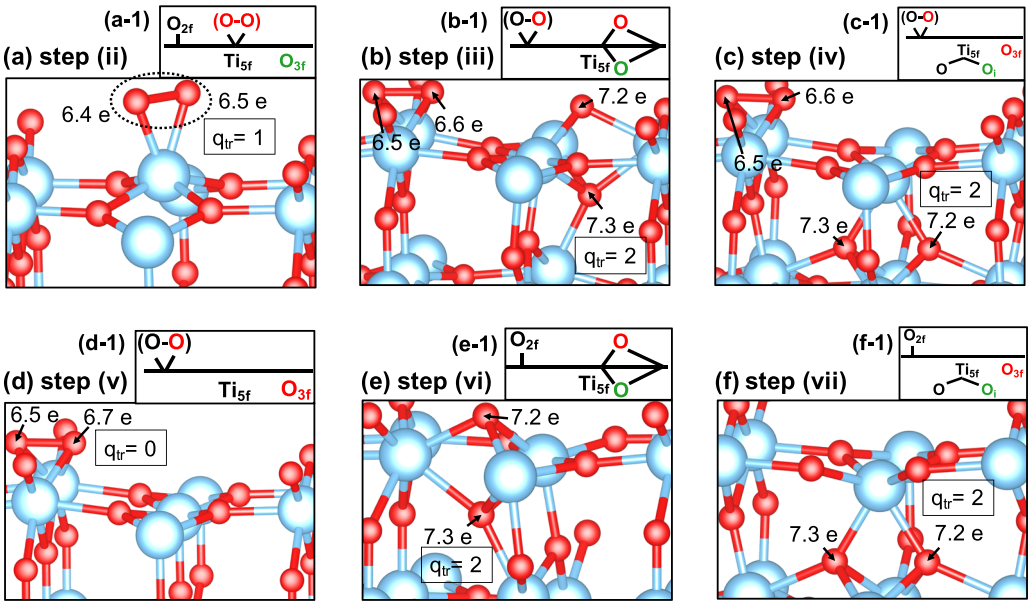

FIG. 3. Sequential steps for the injection of two charged O_i^{2-} through the TiO_2(110) surface, which entails O_2 adsorption, dissociation, and two O injections. (a)–(f) show the reaction intermediates. Annihilation entails movement through the sequence in the reverse order. Insets (a-1)–(f-1) above the atomic geometries show each step schematically; atoms marked in red originate from the gas phase and the blue atom originates from the surface O_{3f} that is exchanged by adsorbates. The configurations shown are as follows: (a) adsorption of O_2 on Ti_{5f}, (b) dissociation of O_2 leaving O_{ads} on both O_{2f} and O_{3f}, resulting in a surface split interstitial above O_{3f}, (c) consecutive motion of the lower O atom from surface split into the subsurface and the higher O atom from surface split into O_{3f}, resulting in a subsurface split interstitial below O_{3f}, (d) diffusion of subsurface split into the deep bulk, (e) formation of the second surface split interstitial above O_{3f} via motion of remaining O_{ads} from O_{2f}, and (f) its injection into the subsurface split below O_{3f}. Note that the initial and final steps, such as step (i) gaseous O_2 and the pristine TiO_2(110) surface and step (viii) diffusion of the second O_i into the deep bulk are omitted here, but they could be referenced from Figs. 1(a) and 1(h), respectively.

charge neutral (q_{tr} = 0), as shown in Fig. 3(d). Then, the subsequent dissociation of the oxygen pair to form a surface split interstitial, as shown in Fig. 3(e), involves the acquisition of the final two electrons.

Figure 4 shows configuration energies for all steps (ii)–(vii) of the injection process plotted as a function of E_F, again under the experimental conditions of our prior O isotope exchange experiments (T = 973 K and P_{O_2} = 1 × 10^{-5} Torr).[18,19,23,25] In Fig. 4, the energies of the neutral configurations shown in Fig. 1 are obtained from Eq. (2) and are independent of the Fermi energy. The energies of the charged configurations shown in Fig. 3 are obtained from Eq. (3) using the inferred value of q_{tr}. These lines appear with negative slope since electron transfer from higher energy electron reservoirs to the surface configurations reduces the overall energy change. Figure 4 highlights that the charge state of a given reaction intermediate depends on the semiconductor Fermi energy. For instance, for step (ii), the reaction intermediate is always expected to be present in the q_{tr} = 1 charge state independent of Fermi energy. On the other hand, for step (iii), the configuration is expected to be neutral for Fermi energies <1.4 eV and otherwise charged (q_{tr} = 2).

In Fig. 5, using the results from Fig. 4, we show the thermodynamic energy landscape "staircase" diagrams for different values of E_F by choosing the lowest energy configuration (neutral or charged) at each step for each Fermi energy. As E_F increases above the VBM, the energy landscape to form $2O_i^{2-}$ becomes more favorable because the high energy electrons from the semiconductor host facilitate many of the elementary steps. For E_F at the CBM, the net energy change is −0.43 eV, making the overall reaction to form interstitials slightly exothermic. Conversely, annihilation of O_i to yield O_2 becomes endothermic.

Figure 5 clearly shows that the energy landscapes vary strongly with E_F. Note that the CBM value of E_F here is shown as 2.4 eV, which corresponds to the bandgap of TiO_2 at the experimental conditions, notably at T = 973 K, and reflects the sharp reduction in the bandgap exhibited by TiO_2 with increasing temperature.[36] Purple arrows in Fig. 5 indicate the largest endothermic energy change along the intermediate steps for each Fermi energy.

In short, three distinct regimes of reaction pathways stand out: For 0 eV < E_F < 0.9 eV (pathway 1), the end products are two neutral O_i injected via surface dumbbells. For 0.9 eV < E_F < 1.3 eV (pathway 2^*), the end products are two charged O_i^{2-} that enter into the interior through surface dumbbells and thereafter pick up electrons from the semiconductor in subsequent steps. The asterisk denotes that pathway 2 is a family of pathways that differ slightly with respect to the specific step in which the electrons are acquired. For 1.3 eV < E_F < 2.4 eV (pathway 3), the end products are two charged O_i^{2-}, and in this case, they enter into the interior through surface splits rather than surface dumbbells.

Overall, Fig. 5 shows that injection is promoted by higher levels of n-type doping in TiO_2. The high n-type character facilitates

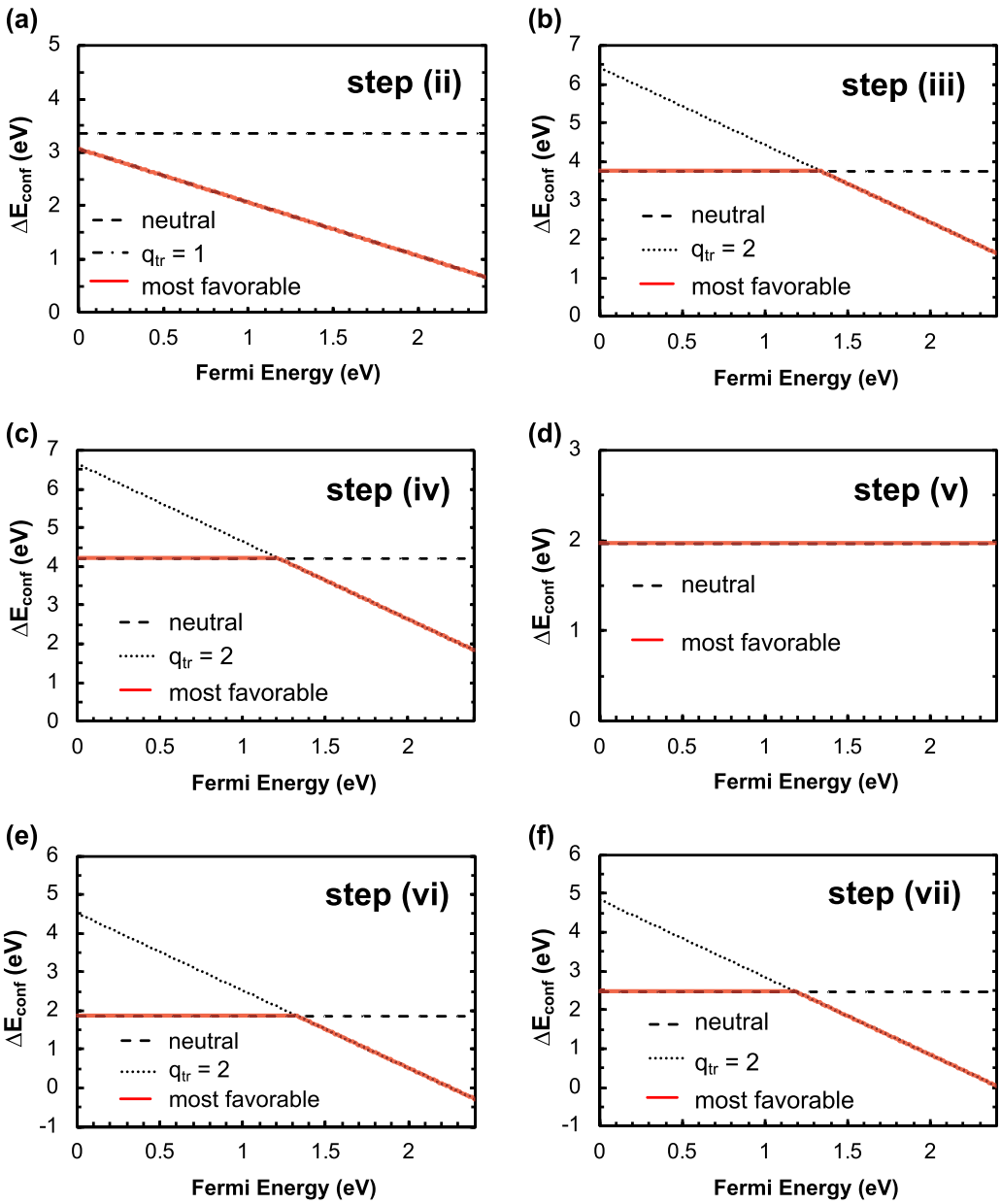

FIG. 4. [(a)–(f)] Surface configuration energies ΔE_{conf} for steps (ii)–(vii), respectively, as a function of Fermi energy at $\Delta\mu_{O_2} = -1.3$ eV (T = 973 K and $P_{O_2} = 1 \times 10^{-5}$ Torr). The black dashed line represents the configuration with no backside vacancy, while the black dotted line represents the configuration with a backside vacancy wherein q_{tr} = 1 or 2. The red solid line represents the most favorable configuration. Transition values between charge states are 1.3 eV for step (iii), 1.2 eV for step (iv), 1.3 eV for step (vi), and 1.2 eV for step (vii).

electron transfer to the O_2 molecule during adsorption and also to forming the surface split during injection. The effects of the latter transfer appear especially clearly in step (vi), which lies significantly downhill of step (v) when the material is n-type [Figs. 5(e) and 5(f)]. Such effects also appear in step (iii) but are amalgamated with unrelated effects of O_2 dissociation and formation of the O_{2f} species.

Figure 5 also shows that annihilation is promoted by the increasingly p-type character of the semiconductor. Orange arrows in Fig. 5 indicate the largest elementary-step changes in

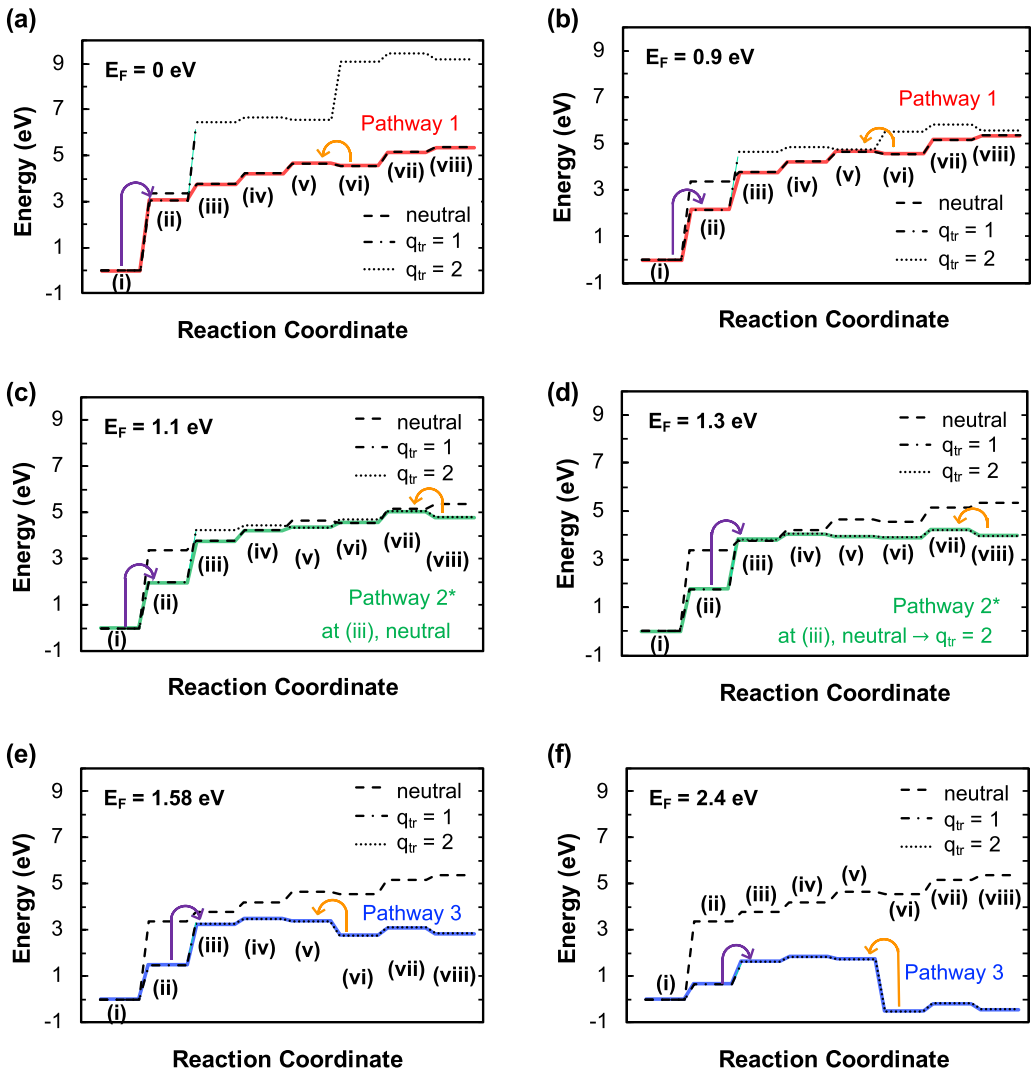

FIG. 5. Energy landscapes for the exchange between O_2 and neutral and charged O_i at representative values of the Fermi energy. Rightward movement along the reaction coordinate corresponds to injection; annihilation proceeds leftward. Across all Fermi energies, exchange follows one of the three pathways. In each diagram, curved arrows indicate the transition exhibiting the highest endothermic energy change for injection (purple) or annihilation (orange). Pathway 1 occurs between (a) $E_F = 0$ eV and (b) $E_F = 0.9$ eV and involves two neutral O_i. The largest uphill step for injection is the initial adsorption of O_2 and for annihilation is formation of O_{2f} from O_{3f}. Pathway 2* represents a family of closely related paths in which $O_{2,ads}$ exists as a surface dumbbell and as O_i^{2-} in the deep bulk and occurs between (c) $E_F = 1.1$ eV and (d) $E_F = 1.3$ eV. Within this range, the largest uphill step for injection changes from the adsorption of O_2 to the dissociation of the O_2 and for annihilation involve the diffusion of O_i^{2-} from the bulk to the 1st sublayer. [(e) and (f)] Pathway 3, in which $O_{2,ads}$ dissociates directly to a surface split and ultimately yields O_i^{2-}, occurs above $E_F = 1.3$ eV. The largest barrier for injection entails the dissociation of O_2 and for annihilation, entails the formation of neutral O_{2f} from charged split O_{3f}.

thermodynamic barrier. Beginning with E_F at the CBM, a large uphill step [(vi) → (v)] stands in the way of O_i seeking to annihilate at the surface, although other smaller steps [(viii) → (vii), (v) → (iv)] also entail uphill climbs for metastable states when charged −2. As E_F declines toward the VBM, the magnitude of the largest uphill transition declines, and increasing fractions of the annihilation pathway become neutral (thereby avoiding larger uphill steps). As noted in Sec. II A, for $E_F < 0.9$ eV, the landscape for annihilation moves almost entirely downhill for neutral O_i.

C. Summary of injection models and limiting thermodynamic barriers

Figure 6 plots the maximum positive thermodynamic energy change required for the entire injection process as a function of E_F over its entire domain 0 eV < E_F < 2.4 eV. This maximum change corresponds to the transitions highlighted by purple arrows shown in Fig. 5. The full domain of Fermi energies 0 eV < E_F < 2.4 eV is broken down into regions representing pathways 1, 2*, and 3.

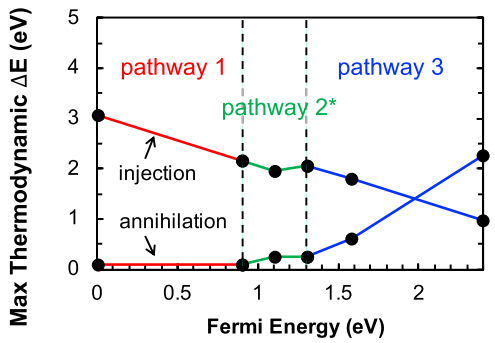

FIG. 6. Maximum endothermic energy change (ΔE) required for the entire injection and annihilation processes as a function of the Fermi energy.

The maximum uphill energy decreases with increasing Fermi energy from 3.07 eV to 0.97 eV across most of the domain. For pathway 1 and partway into pathway 2* up to E_F = 1.2 eV, the maximum energy change originates from the initial molecular O_2 adsorption. Since this adsorption occurs via the transfer of one electron between steps (i) and (ii), the slope in Fig. 6 for pathway 1 equals −1. Partway through the region corresponding to pathway 2* between 1.2 eV < E_F < 1.3 eV, the maximum transition shifts from steps (i) and (ii) to steps (ii) and (iii), which represents the dissociation of $O_{2,ads}$. The maximum energy change increases slightly with a positive slope (+1) in this narrow range because the surface $O_{2,ads}$ bonded to Ti_{5f} returns its excess electrons back to the semiconductor when dissociating to O atoms at an O_{2f} and an O_{3f} site. For pathway 3, the maximum energy change originates from the dissociation of $O_{2,ads}$ to form the surface split [steps (ii) and (iii)]. Since this step involves the transfer of one additional electron from the semiconductor to the adsorbate, the slope in Fig. 6 again equals −1.

Figure 6 also plots the maximum positive thermodynamic energy change for annihilation. This maximum change corresponds to the transitions highlighted by orange arrows shown in Fig. 5 and throughout the domain of E_F corresponds to the transition from step (vi) to (v) involving the movement of O_{ads} from an O_{3f} site to an O_{2f} site. When O_{3f} supports a neutral surface dumbbell, this thermodynamic barrier remains small. But when O_{3f} supports a charged surface split, the barrier increases to 2.25 eV as E_F rises to the CBM because the movement entails the return of two electrons from the adsorbate to the semiconductor.

The present results show that thermodynamic barriers vary with E_F for both injection and annihilation. However, the behavior for these sequences exhibits asymmetry with respect to E_F. The largest elementary-step thermodynamic barrier for interstitial injection trends mostly downward by 2.1 eV as E_F increases between the valence and conduction band edges, while that for annihilation, trends upward by 2.1 eV. This asymmetry represents an energetic manifestation of the fact that the transfer of electrons from the conduction band to the defect becomes easier as the semiconductor becomes more n-type. Indeed, the equilibrium concentration of O_i^{2-} increases as E_F moves toward the conduction band.[23,25]

For our prior experimental conditions (E_F = 1.58 eV),[36] we expect pathway 3 of Fig. 6 to describe the injection sequence. The profile shows a net energy change of 2.85 eV (1.425 eV per O_i^{2-} injected) and an overall modest energy landscape with no transition especially dominant. The highest thermodynamic barriers entails dissociation of the $O_{2,ads}$ [between steps (ii) and (iii)]. However, the present study examines only thermodynamic energy differences. The evaluation of kinetic barriers is necessary for direct comparison and will be described in a forthcoming study.[50]

We have simulated adsorption within a terrace of the (1 × 1) pristine (110) surface that is expected under our experimental condition (T = 973 K and $P_{O_2} = 1 \times 10^{-5}$ Torr).[18,19,23,25] It may be possible to reduce the thermodynamic barrier to adsorption if this step can be modulated in other ways. For example, if the adsorption of O_2 occurs at extended defect sites such as step edges, the adsorption energy may be further reduced due to the lower bond coordination of the ragged step edges.[51–53]

As Fig. S2 in the supplementary material shows, the overall reaction from O_2 to $2O_i$ becomes favorable only for E_F > 2.3 eV. However, the landscapes shown in Fig. 6 end with the formation of O_i in the deep bulk and, therefore, do not encompass the entire range of thermodynamic outcomes available to injected O_i. For example, O_i can react with Ti_i to form various kinds of complexes, platelets, and extended defects, which disappear by the reaction with V_O or reappear at the surface along with Ti_i to extend the bulk lattice. Figure 6 also does not depict entropic contributions to the free energy of O_i at nonzero temperatures; these contributions can be quite large, especially when the defect is ionized.[54] However, Fig. 6 is still useful for estimating the contributions of individual steps to the overall landscape of injection and for assessing the effects of varying E_F.

D. Comparison of injection and ORR

The electron transfer to O_2 in steps (ii) and (iii) is analogous to the well-known oxygen reduction reaction (ORR) in electrochemistry, where O_2 adsorption and dissociation on TiO_2 surfaces occur by electron transfer[55–57] into the antibonding orbitals of the O_2 molecule.[58] The ORR on TiO_2 has stimulated longstanding interest for the photocatalytic activity, photoconductivity, and associated surface phenomena.[55–57,59–63] On titania surfaces, the ORR is believed to occur by sequential electron reduction and in the end produces either superoxide (O^{2-}) in the non-aqueous solution or H_2O_2 and ΔOH in the aqueous solution.[55–57] Recently, Wang *et al.* showed that the concentration of surface-reaching holes determines the rate of the oxygen evolution reaction (OER) as a whole.[64] By analogy, it has been suggested that the rate of the ORR is controlled by the flux of the surface-reaching electrons and is thus associated with the surface Fermi energy.[57,60] The elementary steps considered here, and the sensitivity of the energy change to the Fermi energy, should apply to the steps of the ORR as well.

IV. CONCLUSION

The present work employs first-principles simulations to identify possible pathways for the injection of O_i into the rutile TiO_2 bulk from the gas phase O_2 at a (110) surface. The analysis offers a

better atomistic understanding of our prior isotopic diffusion experiments, highlighting the effects of charge transfer from the semiconductor to the injected oxygen to form two doubly ionized O_i^{2-}. The energy landscape for oxygen injection is sensitive to and can be tuned by the semiconductor Fermi energy. We surmise that E_F may influence defect–surface reaction mechanisms, in general, for semiconducting oxides that support multiple defect charge states having substantially different atomic geometries. Injection via O_2 adsorption, dissociation, and sequential injection is most favorable in n-type TiO_2 where conduction band electrons transferred to the reaction intermediates facilitate the process and reduce thermodynamic energy changes. The reverse process of annihilation occurs most readily in the p-type material. The maximum thermodynamic energy change along the reaction pathway decreases with increasing Fermi energy from around 3 eV to 1 eV for 0 eV < E_F < 2.4 eV. The present study also identifies unexpected split and dumbbell interstitial configurations in the surface plane through which the exchange sequence must pass. These surface species resemble their interstitial analogs in the TiO_2 bulk. The methodology utilized here for computing the dependence of configuration energies on E_F may apply to other oxide semiconductors and prove useful for the analysis of the surface reactions in doped semiconductors by the consideration of the type of dopant, their concentration, and chemical potentials of thermodynamic reservoirs.

SUPPLEMENTARY MATERIAL

See the supplementary material for surface energy vs number of tri-layers in the slab model; total energy change for O_i defects in the TiO_2(110) slab and TiO_2 bulk; description of the "doping" method for simulating the injection of charged O_i^{2-}; determination of charge transfer q_{tr} for reaction intermediates in the presence of backside V_O during injection; effects of Hubbard correction on charge transfer in the presence of backside V_O; and an alternative reaction pathway: the injection of surface oxygen followed by O_2 adsorption.

ACKNOWLEDGMENTS

This work was supported by the U.S. National Science Foundation under Grant No. DMR 17-09327. Computational resources were provided by the Illinois Campus Cluster.

DATA AVAILABILITY

The data that support the findings of this study are available from the corresponding author upon reasonable request.

REFERENCES

[1] V. Binas, D. Venieri, D. Kotzias, and G. Kiriakidis, J. Mater. **3**, 3 (2017).
[2] M. Ge, J. Cai, J. Iocozzia, C. Cao, J. Huang, X. Zhang, J. Shen, S. Wang, S. Zhang, K.-Q. Zhang, Y. Lai, and Z. Lin, Int. J. Hydrogen Energy **42**, 8418 (2017).
[3] B. Karunagaran, P. Uthirakumar, S. J. Chung, S. Velumani, and E.-K. Suh, Mater. Charact. **58**, 680 (2007).
[4] J. Zhang, Z. Qin, D. Zeng, and C. Xie, Phys. Chem. Chem. Phys. **19**, 6313 (2017).
[5] P. Ravirajan, S. A. Haque, J. R. Durrant, D. D. C. Bradley, and J. Nelson, Adv. Funct. Mater. **15**, 609 (2005).
[6] L. Zhang, J. M. Cole, and C. Dai, ACS Appl. Mater. Interfaces **6**, 7535 (2014).
[7] M. A. Henderson, W. S. Epling, C. L. Perkins, C. H. F. Peden, and U. Diebold, J. Phys. Chem. B **103**, 5328 (1999).
[8] M. D. Rasmussen, L. M. Molina, and B. Hammer, J. Chem. Phys. **120**, 988 (2004).
[9] Y. Wang, D. Pillay, and G. S. Hwang, Phys. Rev. B **70**, 193410 (2004).
[10] A. C. Papageorgiou, N. S. Beglitis, C. L. Pang, G. Teobaldi, G. Cabailh, Q. Chen, A. J. Fisher, W. A. Hofer, and G. Thornton, Proc. Natl. Acad. Sci. U. S. A. **107**, 2391 (2010).
[11] I. Sokolović, M. Reticcioli, M. Čalkovský, M. Wagner, M. Schmid, C. Franchini, U. Diebold, and M. Setvín, Proc. Natl. Acad. Sci. U. S. A. **117**, 14827 (2020).
[12] Z. Zhang and J. T. Yates, Jr., Surf. Sci. **652**, 195 (2016).
[13] G. Hu, Z. Wu, and D.-e. Jiang, J. Phys. Chem. C **122**, 20323 (2018).
[14] Y. Zhao, Z. Wang, X. Cui, T. Huang, B. Wang, Y. Luo, J. Yang, and J. Hou, J. Am. Chem. Soc. **131**, 7958 (2009).
[15] M. Reticcioli, I. Sokolović, M. Schmid, U. Diebold, M. Setvin, and C. Franchini, Phys. Rev. Lett. **122**, 016805 (2019).
[16] S. Tan, H. Feng, Y. Ji, Q. Zheng, Y. Shi, J. Zhao, A. Zhao, J. Yang, Y. Luo, B. Wang, and J. G. Hou, J. Phys. Chem. C **122**, 28805 (2018).
[17] R. Zhang, H. Wang, X. Peng, R.-r. Feng, A.-a. Liu, Q. Guo, C. Zhou, Z. Ma, X. Yang, Y. Jiang, and Z. Ren, J. Phys. Chem. C **123**, 9993 (2019).
[18] A. G. Hollister, P. Gorai, and E. G. Seebauer, Appl. Phys. Lett. **102**, 231601 (2013).
[19] P. Gorai, A. G. Hollister, K. Pangan-Okimoto, and E. G. Seebauer, Appl. Phys. Lett. **104**, 191602 (2014).
[20] P. Gorai, E. Ertekin, and E. G. Seebauer, Appl. Phys. Lett. **108**, 241603 (2016).
[21] M. Li and E. G. Seebauer, J. Phys. Chem. C **120**, 23675 (2016).
[22] K. L. Gilliard and E. G. Seebauer, J. Phys.: Condens. Matter **29**, 445002 (2017).
[23] K. M. Pangan-Okimoto, P. Gorai, A. G. Hollister, and E. G. Seebauer, J. Phys. Chem. C **119**, 9955 (2015).
[24] K. L. Gilliard-AbdulAziz and E. G. Seebauer, Phys. Chem. Chem. Phys. **20**, 4587 (2018).
[25] K. L. Gilliard-AbdulAziz and E. G. Seebauer, Appl. Surf. Sci. **470**, 854 (2019).
[26] M. Li and E. G. Seebauer, J. Phys. Chem. C **122**, 2127 (2018).
[27] P. A. Mulheran, M. Nolan, C. S. Browne, M. Basham, E. Sanville, and R. A. Bennett, Phys. Chem. Chem. Phys. **12**, 9763 (2010).
[28] B. Wen, W.-J. Yin, A. Selloni, and L.-M. Liu, J. Phys. Chem. Lett. **9**, 5281 (2018).
[29] J. Gaberle and A. Shluger, RSC Adv. **9**, 12182 (2019).
[30] G. Kresse and J. Furthmüller, Comput. Mater. Sci. **6**, 15 (1996).
[31] G. Kresse and J. Furthmüller, Phys. Rev. B **54**, 11169 (1996).
[32] G. Kresse and D. Joubert, Phys. Rev. B **59**, 1758 (1999).
[33] J. P. Perdew, K. Burke, and M. Ernzerhof, Phys. Rev. Lett. **77**, 3865 (1996).
[34] P. M. Kowalski, B. Meyer, and D. Marx, Phys. Rev. B **79**, 115410 (2009).
[35] S. Zhang and J. Northrup, Phys. Rev. Lett. **67**, 2339 (1991).
[36] H. Jeong, E. G. Seebauer, and E. Ertekin, Phys. Chem. Chem. Phys. **20**, 17448 (2018).
[37] S. Lany and A. Zunger, Phys. Rev. B **78**, 235104 (2008).
[38] A. Janotti, J. B. Varley, P. Rinke, N. Umezawa, G. Kresse, and C. G. Van de Walle, Phys. Rev. B **81**, 085212 (2010).
[39] H.-Y. Lee, S. J. Clark, and J. Robertson, Phys. Rev. B **86**, 075209 (2012).
[40] H.-P. Komsa and A. Pasquarello, Phys. Rev. Lett. **110**, 095505 (2013).
[41] D. Wang, D. Han, X.-B. Li, S.-Y. Xie, N.-K. Chen, W. Q. Tian, D. West, H.-B. Sun, and S. B. Zhang, Phys. Rev. Lett. **114**, 196801 (2015).
[42] C. Freysoldt and J. Neugebauer, Phys. Rev. B **97**, 205425 (2018).
[43] R. Löfgren, R. Pawar, S. Öberg, and J. A. Larsson, New J. Phys. **20**, 023002 (2018).
[44] R. Löfgren, R. Pawar, S. Öberg, and J. A. Larsson, New J. Phys. **21**, 053037 (2019).
[45] H. Li, Y. Guo, and J. Robertson, J. Phys. Chem. C **119**, 18160 (2015).
[46] Y.-F. Li, Z.-P. Liu, L. Liu, and W. Gao, J. Am. Chem. Soc. **132**, 13008 (2010).
[47] A. A. Iyer and E. Ertekin, Phys. Chem. Chem. Phys. **19**, 5870 (2017).

[48]N. Kim, E. M. Turner, Y. Kim, S. Ida, H. Hagiwara, T. Ishihara, and E. Ertekin, J. Phys. Chem. C **121**, 19201 (2017).
[49]Á. Valdés, Z.-W. Qu, G.-J. Kroes, J. Rossmeisl, and J. K. Nørskov, J. Phys. Chem. C **112**, 9872 (2008).
[50]H. Jeong, E. Ertekin, and E. G. Seebauer, "Kinetic Control of Oxygen Interstitial Interaction with TiO_2(110) via the Surface Fermi Energy" (unpublished).
[51]H. Onishi, K.-i. Fukui, and Y. Iwasawa, Bull. Chem. Soc. Jpn. **68**, 2447 (1995).
[52]S. Fischer, A. W. Munz, K.-D. Schierbaum, and W. Göpel, Surf. Sci. **337**, 17 (1995).
[53]U. Diebold, J. Lehman, T. Mahmoud, M. Kuhn, G. Leonardelli, W. Hebenstreit, M. Schmid, and P. Varga, Surf. Sci. **411**, 137 (1998).
[54]J. A. Van Vechten and C. D. Thurmond, Phys. Rev. B **14**, 3539 (1976).
[55]C. M. Wang, A. Heller, and H. Gerischer, J. Am. Chem. Soc. **114**, 5230 (1992).
[56]M. Kaneko, J. Nemoto, H. Ueno, N. Gokan, K. Ohnuki, M. Horikawa, R. Saito, and T. Shibata, Electrochem. Commun. **8**, 336 (2006).
[57]H. Sheng, H. Ji, W. Ma, C. Chen, and J. Zhao, Angew. Chem., Int. Ed. **52**, 9686 (2013).
[58]Y.-F. Li, U. Aschauer, J. Chen, and A. Selloni, Acc. Chem. Res. **47**, 3361 (2014).
[59]A. Tsujiko, H. Itoh, T. Kisumi, A. Shiga, K. Murakoshi, and Y. Nakato, J. Phys. Chem. B **106**, 5878 (2002).
[60]A. Fujishima, X. Zhang, and D. Tryk, Surf. Sci. Rep. **63**, 515 (2008).
[61]D.-N. Pei, L. Gong, A.-Y. Zhang, X. Zhang, J.-J. Chen, Y. Mu, and H.-Q. Yu, Nat. Commun. **6**, 8696 (2015).
[62]F.-Y. Hsieh, L. Tao, Y. Wei, S.-h. Hsu, J. Rick, J.-F. Lee, Y.-W. Yang, and B.-J. Hwang, NPG Asia Mater. **9**, e403 (2017).
[63]S. Tominaka, A. Ishihara, T. Nagai, and K.-i. Ota, ACS Omega **2**, 5209 (2017).
[64]D. Wang, T. Sheng, J. Chen, H.-F. Wang, and P. Hu, Nat. Catal. **1**, 291 (2018).